Spatiotemporal analysis of extreme precipitation and sea surface temperature events in the northern hemisphere via complex network theory

by

Connor Saari

B.S., Brigham Young University - Idaho, 2023

A THESIS

submitted in partial fulfillment of the requirements for the degree

MASTER OF SCIENCE

Department of Geology
College of Arts and Sciences

KANSAS STATE UNIVERSITY
Manhattan, Kansas

2025

Approved by:

Co-Major Professor
Dr. Matthew Kirk

Approved by:

Co-Major Professor
Dr. Behzad Ghanbarian

Copyright

Abstract

Climate variables can be synchronized across broad spatial and temporal scales, with regional, continental, and global patterns. Investigating the topological patterns and underlying mechanisms of extreme precipitation and sea surface temperature events (EPEs and ESSTEs) is crucial to forecast weather conditions and understand the impacts of climate change on natural hazards, such as floods and hurricanes. In the study, we propose integrative spatiotemporal analysis of inland EPEs and ESSTEs to better understand our dynamic atmosphere in the face of global climate change. More specifically, we focus on the region between 0 and 60 degrees latitude in the northern hemisphere. We collected gridded gauge-and-interpolation-based monthly precipitation and temperature data from 1930 to 2020 and detected extreme events based on the 95^{th} percentile threshold. To quantify synchronization between extreme events, we used the event synchronization (ES) method and applied a null model distribution to ensure that links were non-random. We then constructed EPEs and ESSTEs complex networks and calculated different network metrics including degree centrality, mean geographic distance and clustering coefficient. Results showed that the frequency of extreme precipitation and sea surface temperature events increased over the past nine decades, with significant spatial variability. Key synchronization hubs emerged in Mexico, the African Sahel, and parts of Asia for precipitation, while extreme SST events were concentrated in regions influenced by major ocean currents, highlighting distinct spatial patterns for terrestrial and marine extremes.

Table of Contents

List of Figures

Acknowledgements

The process of earning a master's degree, and the following thesis has been one of the more challenging experiences I've had in my life and would not be possible without the help of many people here at this school.

Before any other, one person deserves recognition and my most sincere thanks: my advisor, Dr. Behzad Ghanbarian. Without your expert guidance, correction, and monstrous work ethic throughout my studies here at K-State, I would never have reached this point. I owe a large part of who and where I am to you, thank you.

Also of much influence are my committee members, Dr. Pascal Hitzler, and Dr. Matthew Kirk, who doubles as my co-major advisor during the latter half of my time here. The insight, and valuable professional perspectives were helpful along the way to forming my research.
On a more personal level, I am grateful for the companionship and welcome I received from Kehinde Bosikun and Victor Oladoja during my first year, with special mention to Tayeb Jamali for key assistance within the course of this research. Our weekly research meetings held with Dr. Ghanbarian provided confidence and skills key to clearly presenting my work. Your help in formatting my writing, learning python programming, and understanding complex network theory saved me much grief on this journey. Our meetings outside of school provided me joy, and an expanded perspective.

Also important to my development at this university are the many wonderful instructors, some of whom which have since moved to other schools to the great loss of K-State. Drs. Abdelmoneam Raef, Claudia Adam, Cen Wu, Lior Shamir, Karin Goldberg, Matthew Kirk, and Behzad Ghanbarian. Their knowledge, passion, and dedication to providing excellent learning opportunities has made this a truly enjoyable experience.

I would like to extend my appreciation to Kansas State University for creating a space of excellence and a culture of success in which I could thrive. I am also supremely grateful to the Department of Geology and the K-State Graduate School for the financial support they so generously offered me which allowed me to devote my entire mind to the pursuit of my studies.

Last, I am grateful for my fellow students, my new friends, those at home, and my family. Your encouraging words, academic insights, and comradery have made it all worth it, and my life here has been greatly enriched.

We acknowledge the use of ChatGPT 3.5 for language editing and proofreading of this manuscript. The AI was used to improve grammar, clarity, and readability. All intellectual contributions, data interpretation, and conclusions remain the sole responsibility of the authors

Dedication

I dedicate this work to my family: Russell, Teresa, Cassi, Wesley, Kara, and to my wife Whitnee. Knowing that there was always someone to guide me or a shoulder to lean on was at times the only thing that kept me going. Thank you.

Chapter 1 - Introduction

Precipitation, particularly rainfall, is a fundamental component of the hydrologic cycle and is intricately linked to sea surface temperature (SST) (Alexander et al., 2009; Van Der Ent et al., 2013). These climate variables serve as primary drivers of atmospheric and oceanic processes across multiple spatial scales, influencing ecosystems, agriculture, infrastructure, and weather patterns. The interconnecting between precipitation and SST is particularly significant in the context of extreme events, as changes in SST can modulate atmospheric moisture content, leading to enhanced or suppressed precipitation patterns (Kotz et al., 2022). Understanding the mechanisms governing these interactions is critical for predicting extreme weather events and mitigating their socio-economic impacts.

Recent climate studies have highlighted the growing influence of anthropogenic climate change on the frequency and intensity of extreme precipitation and SST events (EPEs and ESSTEs). Global warming has been associated with shifts in precipitation regimes, with increased rainfall intensity and altered spatial distributions (Diffenbaugh et al., 2017). Similarly, SST anomalies contribute to atmospheric instability and convection, playing a pivotal role in modulating precipitation events (Roxy, 2014). These changes have far-reaching consequences, influencing flood risks, drought occurrences, and hurricane development (Walsh et al., 2016).

Traditional statistical methods, such as empirical orthogonal functions, have been widely used to analyze spatiotemporal variations in climate data (Hannachi, 2004). However, these approaches often struggle to capture the propagation of extreme events within complex climate systems. In contrast, complex network theory provides a powerful framework for analyzing climate interactions by revealing synchronization patterns and identifying key regions of influence (Donner et al., 2010). Recent applications of network-based analyses have

demonstrated their effectiveness in uncovering dominant co-variability patterns between SST and precipitation, thereby offering new insights into their interdependencies (Stolbova et al., 2020).

This study employs complex network theory to investigate the synchronization of EPEs and ESSTEs in the Northern Hemisphere, focusing on the region between 0° and 60° latitude. By leveraging long-term, high-resolution datasets, we aim to quantify the spatiotemporal relationships of these extreme events, assess their connectivity, and identify potential teleconnection mechanisms. The overarching goal is to improve our understanding of how climate extremes propagate and interact at regional and global scales, thereby enhancing predictive modeling efforts for extreme weather events.

1.1 Climate setting

The study region, spanning from the equator to 60°N latitude, encompasses diverse climatic zones influenced by both atmospheric and oceanic processes. The Northern Hemisphere exhibits a complex interplay between land, ocean, and atmospheric dynamics, leading to varied precipitation patterns and SST variations. Key climate drivers include monsoonal systems, atmospheric circulation patterns, and ocean currents, all of which contribute to regional and seasonal variability in extreme events.

The tropical and subtropical regions within the study domain experience strong atmospheric convection driven by SST anomalies. The presence of the Intertropical Convergence Zone (ITCZ) significantly influences precipitation patterns, particularly in regions such as the African Sahel and parts of South Asia (Nicholson, 2013). The El Niño-Southern Oscillation (ENSO) also exerts a pronounced impact on precipitation variability, with El Niño conditions

typically leading to anomalous rainfall in some areas while causing droughts in others (Sun and Furbish, 1997).

Further north, mid-latitude climate dynamics are shaped by extratropical cyclones, atmospheric wave patterns, and the influence of major ocean currents such as the Gulf Stream and Kuroshio Current. These currents regulate SST distributions and, consequently, atmospheric moisture transport, affecting precipitation extremes along coastal and inland regions. In particular, SST anomalies in the North Atlantic and North Pacific have been linked to variability in storm tracks and precipitation extremes in Europe, North America, and East Asia (Deser et al., 2010).

The seasonal cycle plays a crucial role in the occurrence of extreme events. The majority of hurricanes and intense precipitation episodes in the Northern Hemisphere occur between June and November, coinciding with peak SSTs and atmospheric instability. The study, therefore, focuses on this six-month period (JJASON) to capture the most significant interactions between EPEs and ESSTEs.

Overall, the climate setting of this study underscores the importance of understanding SST-precipitation linkages within a broader climatological framework. By integrating complex network analysis with climate data, this research aims to uncover the synchronization structures that govern extreme event propagation, ultimately contributing to improved hazard prediction and climate adaptation strategies.

Chapter 2 - Materials and Methods

2.1 Data

The monthly sea surface temperature (SST) data used in this study were collected from the Berkley Earth's Global Gridded Temperature database that consists of approximately 16000 nodes globally, with a resolution of 1˚ × 1 ˚ and a temporal range of 1850 – 2020. The monthly precipitation data were collected from the Global Precipitation Climatology Center (GPCC) database and include data from 1891 to 2020 with the 1˚ × 1 ˚ resolution. These two databases were selected because of their overlapping time frames, spatial resolution, and reporting frequency. Pre-processing analyses showed substantial uncertainties in the interpolated monthly precipitation data before 1930, and, thus, the data were trimmed to the years 1930 through 2020. After pre-processing, we ended with 8516 and 13083 grid points for the precipitation and sea surface temperature networks, respectively, in the Northern Hemisphere.

We only analyzed the precipitation and SST data from June to November (hereafter JJASON). Based on NOAA's Tropical Cyclone Climatology report, most hurricanes in the Northern hemisphere happen from June to November. We, therefore, restrict our data analysis to this 6-month period.

2.2 Network Construction

2.2.1 Extreme Precipitation and Sea Surface Temperature Events

There are various methods, such as extreme value theory (Buishand, 1989), to identify the extremity of events in time series data. However, for the sake of simplicity, we applied the threshold approach. More specifically, we assumed that precipitation, and SST events with values above the 95th percentile of all months were extremes at each node. Using the 95th

percentile threshold, we constructed the extreme precipitation and SST events (EPEs and ESSTEs) series composed of zeros and ones representing respectively non-extreme and extreme events. This is because our focus was on the number of extreme events and their synchronizations not their magnitudes.

2.2.2 Event Synchronization

To calculate the level of similarity between two extreme event series and measure the synchronization of extreme events between the nodes, we used the event synchronization (ES) method (Malik et al., 2011). The degree of similarity between any pair of grid points waw computed by counting the number of synchronized events for each pair and using the time delay $\Delta_{m,n}^{i,j}$ that meets the condition of $\left|\Delta_{m,n}^{i,j}\right| < \tau_{m,n}^{i,j}$ and $\left|\Delta_{m,n}^{i,j}\right| \leq \tau_{m,n}^{i,j}$. $\Delta_{m,n}^{i,j}$ and $\tau_{m,n}^{i,j}$ are defined as

$$\Delta_{m,n}^{i,j} = t_n^j - t_m^i \quad (1)$$

$$\tau_{m,n}^{i,j} = \frac{1}{2} * \min\{\Delta_{m,m-1}^{i,i}, \Delta_{m,m+1}^{i,i}, \Delta_{n,n-1}^{j,j}, \Delta_{n,n+1}^{j,j}\} \quad (2)$$

where $\tau_{m,n}^{i,j}$ is the local time scale, which may change depending on extreme events. Within the ES method τ_{max} constrains $\Delta_{m,n}^{i,j}$ to maintain realistic synchronization between events (Boers et al., 2014). In this study, we set τ_{max} = 0, to analyze the EPEs and ESSTEs occurring within the same month in the Northern hemisphere. Using the ES values, the similarity matrix contained the degree of synchronization among the nodes was then created.

2.2.3 Adjacency

To establish statistically-meaningful links among the nodes and accurately compute the adjacency matrix composed of zeros (no links) and ones (representing links), we used a null-model distribution. To minimize the bias associated to random links, we shuffled each extreme event series 1000 times and then calculated the ES value via the event synchronization method.

Then, the distribution of the calculated ES values was analyzed at each node. For this purpose, we determined the 99.5th percentile threshold for each pair nodes and computed the corresponding ES value i.e., ES_{thresh}^{ij}. If the ES value determined based on the original (unshuffled) extreme event series was greater than the threshold ES value, then a link was established between those two nodes and the corresponding element in the adjacency matrix was set equal to one. This approach was used to maintain quality control and establish only connections not caused by coincidence or by inherent biases caused by event rate differences in the nodes time series.

2.3 Network Measures

In this section, we briefly describe several network measures i.e., degree centrality, mean geographic distance and clustering coefficient, commonly used in the complex network literature (Donges et al., 2009, Jamali et al., 2023, Feldhoff et al., 2014), and explain how we use them to analyze the spatiotemporal patterns of the EPE and ESSTE.

2.3.1 Degree Centrality

The degree of node *i* (k_i) represents the number of connections that it has with other nodes. In other words, k_i indicates the magnitude of connectivity. This metric measures the importance of a node within the network structure. Specifically, in our context, it reflects the level of association between extreme events occurring at a particular node and those at other nodes. To gain insights into the propagation dynamics within the constructed networks, we calculated k_i as follows:

$$k_i = \sum_{j=1}^{N} A_{(i,j)} \tag{3}$$

where N represents the total number of nodes in the network. Nodes with high degrees are called hubs. In climate networks, nodes with high degrees represent important locations for propagation or teleconnection.

2.3.2 Mean Geographical Distance

The mean geographical distance (MGD) quantifies the average spatial separation between a node and its connected neighbors. This metric assesses whether a node extreme patterns are more closely aligned with nearby regions or with distant areas. A higher MGD suggests that the node is involved in teleconnections – long-distance climate interactions – while a lower MGD indicates influence confined to local geographic regions. The MGD is given by

$$MGD_i = \frac{1}{k_i} \sum_{j=1}^{n} D_{(i,j)} N_{(i,j)} \tag{4}$$

where $D_{(i,j)}$ is the geographic distance between nodes i and j and $N_{(i,j)}$ denotes the set of neighbors of node i. We used the MGD, along with our other network measures, to determine the localities of influence among the nodes.

2.3.3 Clustering Coefficient

The clustering coefficient (C_i) provides insights into the extent to which neighbors of a specific node are interconnected, offering a measure of local link density. Clustering coefficient measures how many nodes that share links with a specified node are connected. The value of CC at node i is determined as follows:

$$C_i = \frac{2L_i}{\mathrm{k(k-1)}} \tag{5}$$

where L_i is the number of links among k neighbors of node i. The C_i ranges between 0, indicating no connections among the neighbors of node i, and 1, signifying that all neighbors of node i are interconnected. C_i may be used as a measure of spatial coherency for the occurrence of

our ESSTEs and EPEs. Clustering coefficients approaching 0 in a location is interpreted as having low spatial coherency, meaning any event which occurs at a given node would likely not have a significant effect on the surrounding nodes. Conversely, a high C_i which approaches a value of 1 is interpreted as having a high degree of spatial coherency and means that local events are likely to have some influence on connected nodes.

2.4 Spatial Significance of Network Measures

At scales less than global (e.g., national, continental or semi-global), the accuracy of climate networks can be influenced by boundaries. Nodes inside a climate network, particularly those near the edges of boundaries, may connect with others across boundaries. For instance, nodes in our study, particularly those located near the equator, might have connections to nodes in the Southern Hemisphere, which would skew the analysis of our ESSTE and EPE networks. To minimize such boundary effects, we applied a normalization method proposed and successfully evaluated by Rheinwalt et al. (2012). This approach involves correcting network measures by normalizing each node's value against the expected value derived from surrogate networks. To make such corrections, we generated 1000 surrogate networks, randomizing the values of the original networks, but keeping the structures intact. The original values were then subtracted by the average value of the surrogated networks. This technique is used to minimize biases related to the boundary effect, ensuring more accuracy in representing our node-level dynamics.

Chapter 3 - Results and Discussion

3.1 Precipitation and Sea Surface Temperature Data Analysis

To analyze the overall temporal trend in the number of extreme events in the Northern Hemisphere, we first plotted the number of extreme events versus the year and performed some regression analysis to detect the trends in the EPEs and ESSTEs. For this purpose, we included all data from all nodes regardless of their locations. More specifically, we conducted both linear and Poisson regressions, as shown in Fig. 1. For this work, we present the results for the most recent 40 years. Although the plots look scattered, as can be observed, the general trends in the data over 40 years (1980-2020) are increasing for both EPEs count and ESSTEs.

We used the Kolmogorov-Smirnov test to evaluate whether the data followed a specific distribution or trend before selecting an appropriate regression model. When we applied the KS test, we found that neither regression model fit the overall trend of our data, which we attribute to the overall non-linear trend of the data.

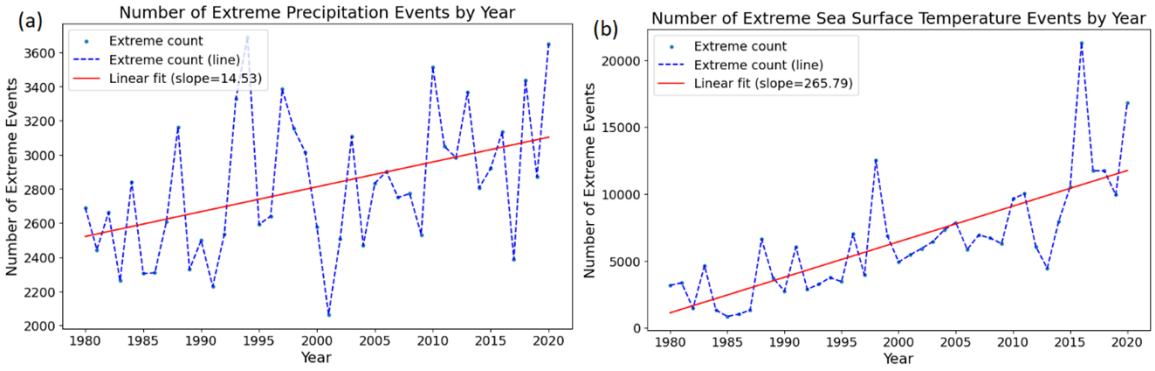

Figure 1 Number of EPEs (left) and number of ESSTEs (right) as a function of year. The red solid line represents the fit of the linear model to the data. The dashed blue lines is for the sake of the visibility of yearly changes.

Our results in Fig. 1 align with those of Alexander (2016), who reported an increase in the proportion of the Northern Hemisphere experiencing a rising percentage of extreme precipitation events (EPEs). Our ESSTE data aligns with findings from the Copernicus Climate

Change Service, which reported record-breaking North Atlantic Sea surface temperatures contributing to extreme marine heatwaves in recent years. These increasing extreme SST events reflect broader trends of rising ocean temperatures, which may influence the frequency and intensity of extreme precipitation events.

To detect which regions in the Northern Hemisphere have been significantly impacted by extreme events over time, we further analyzed the number of extreme events at each node and their trends via linear and Poisson regressions. For this purpose, we plotted the number of extreme events against the year, fit both a linear and Poisson regression to the data at each node and then investigated whether the slope was significantly positive or negative via t-test at the significance level of 0.05.

Results for the EPEs are presented in Figs. 2a and 2b in which nodes with statistically significant positive slopes are shown via the blue dots, while those with statistically significant negative slopes via the orange dots. The black dots represent the nodes with statistically non-significant (zero) slopes. Blue dots in Fig. 2a refer to some regions in Russia, west China, Pakistan, Afghanistan, Saudi Arabia, Iran, Turkey and in Asia, Niger, Mali, Ethiopia, and Somalia in Africa, Ukraine and Spain in Europe, Mexico, Texas (US) and North and North East of Canada in North America. The results of our statistical analysis shown in Fig. 2a are consistent with some recent severe floods around the world, such as Middle East (Shehzad, 2023), Texas (Green et al., 2025), west China (Wang et al., 2025). For instance, Zittis et al. (2022) reported the Eastern Mediterranean and Middle East region as an important climate change hotspot. Those authors highlighted that greenhouse gas emissions in this region are rising rapidly and exceeding those of the European Union. Zittis et al. (2022) noticed that the region has experienced accelerated warming compared to other inhabited areas, particularly in recent

decades, with an average increase of approximately 0.45°C per decade. Additionally, evident shifts in the hydrological cycle and increasing occurrences of extreme weather events pose major societal challenges including more intense rainfall events capable of triggering flash floods (Zittis et al., 2022).

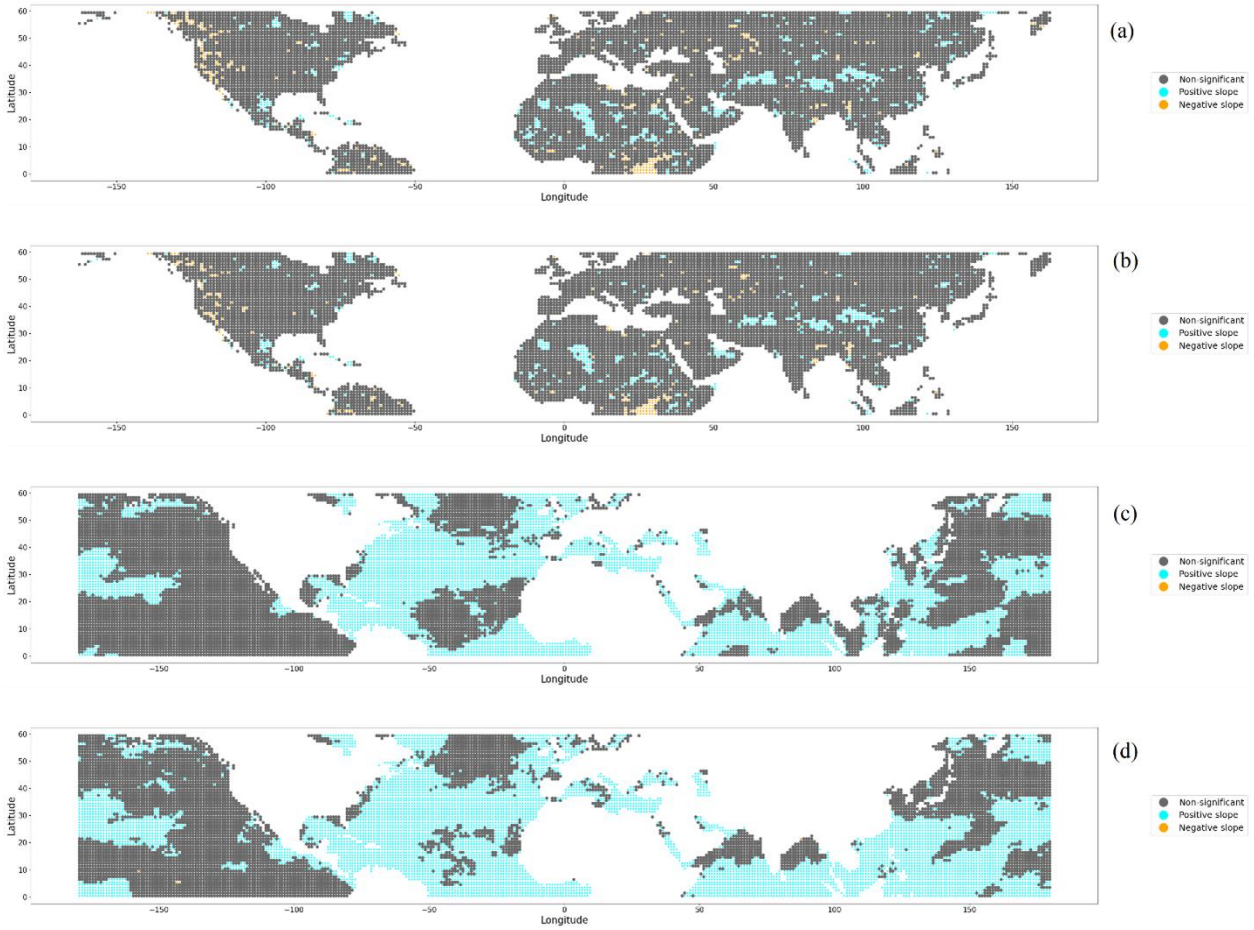

Figure 2 Node-based trends in the EPEs based on (a) linear and (b) Poisson regressions for the land masses within the study area of 0˚N to 60˚N. Node-based trends in the ESSTEs based on (c) linear and (d) Poisson regressions for the seas/oceans within the study area of 0˚N to 60˚N. Blue dots represent statistically significant increase in trend, while the orange dots denote the oppositive. White dots represent no significant change.

As we showed in Figs. 2c and 2d, numerous regions in the seas and oceans in the Northern Hemisphere have significantly positive increasing trends in the number of ESSTEs, particularly in the Pacific Ocean, Indian Ocean, and Atlantic Ocean. Our results are in accord with those reported by Merchant et al. (2025) who found that the global mean sea surface

temperature increased from 0.06°C per decade during 1985-1989 to 0.27°C per decade between 2019 and 2023, which indicates a more than fourfold acceleration in ocean warming.

3.2 Network Measures

In the following sections, we present the results of complex network theory and more specifically network measures obtained by analyzing the EPEs and ESSTEs within the Northern Hemisphere during the defined months of JJASON. Recall that all network measures were corrected due to spatial boundary effect into account and therefore normalized and ranged between 0 and 1. We should point out that we set τ_{max} = 0 meaning that our results are based on the extreme events synchronized within the same month. Therefore, those synchronous events happened at greater time scales (more than a month) were not analyzed in this study.

3.2.1. Degree

Degree, k,is a fundamental measure that quantifies the importance of a node based on the number of its direct connections to other nodes in a network. A node with high degree has many direct connections (known as hub or super node), while a node with low degree has few connections and therefore is isolated.

Figure 3 presents the degree values for both the EPE and ESSTE networks constructed using $\tau_{max} = 0$. As can be seen, high degree values are observed in both networks. Recall that regions with high degrees (known as hubs) are indicative of locations where EPEs or ESSTEs occur synchronously with many other locations.

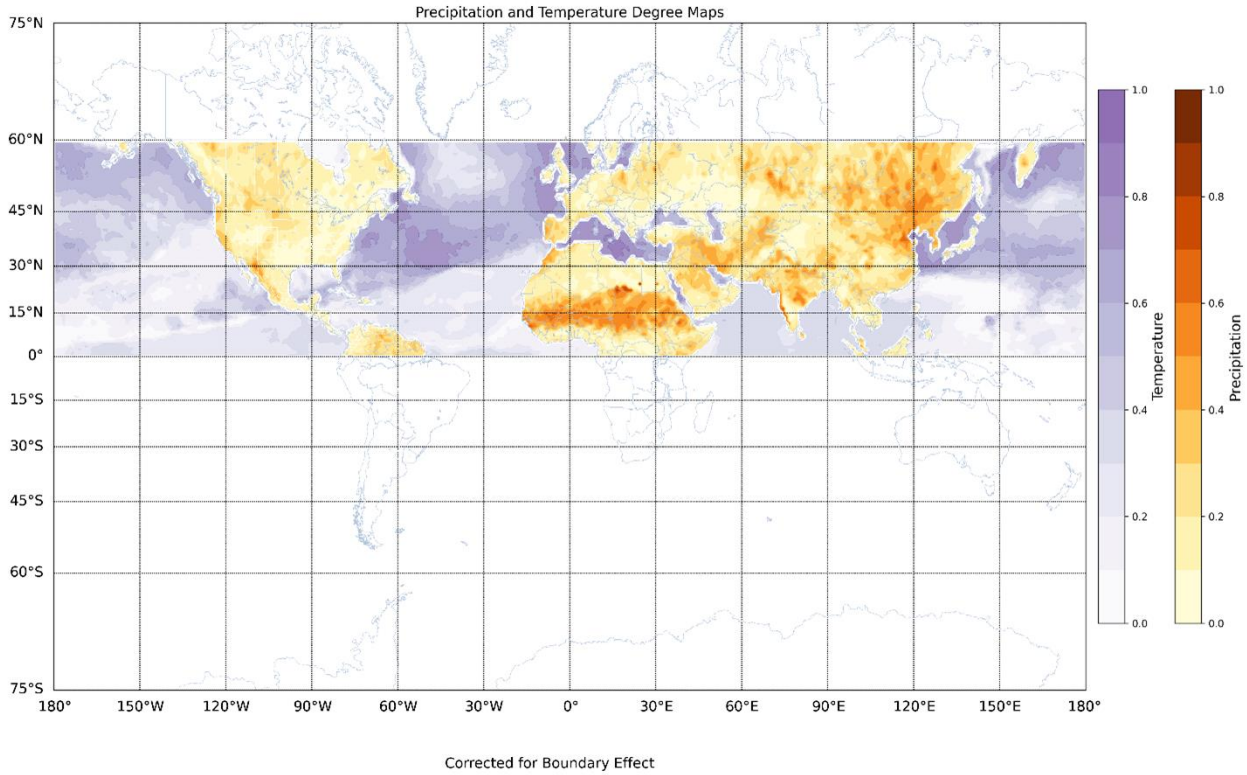

Figure 3 Degree values, corrected for spatial boundary effects, within the Northern Hemisphere (0-60° north) for data from 1930 to 2020. Results for the EPEs are shown with warm tones (right scale), while for the ESSTEs with cool tones (left scale.) The numerical scale is the same for both, ranging from 0 to 1. The map outside of the study area is empty and used only to show relation to the study area.

Hubs within the EPE network include Northwestern Mexico, the Southwestern coast of India, Central to Eastern China (as seen in Wang et al., 2023) and Mongolia, as well as some regions in Southeastern Russia and Northern Kazakhstan. We also observed high k values in the African Sahel—a semiarid region extending from the Atlantic Ocean to the Red Sea, encompassing countries such as Senegal, Mali, Niger, Chad, and Sudan. This region, acting as a transitional zone between the Sahara Desert and more fertile savannas, is characterized by a harsh climate with seasonal rainfall and sparse vegetation. The Sahel is remarkably dry and arid, where minimal precipitation is evenly distributed across vast continental areas with rare small-scale extreme events. The low precipitation gradient here leads to high connectivity across large spatial scales. Hubs detected in the Sahel (Fig. 3) are consistent with those reported by

Scarsoglio et al. (2013), who used monthly precipitation data from 1941 to 2020 in the GPCC database. More specifically, they constructed the complex network using the precipitation data (not extreme values) and reported high degrees in Sahel, Eastern Australia and Northern Europe (see their Fig. 2).

The African Sahel is close to the equator, the lower boundary in our study restricted to the region between 0 and 60° north. Finding results consistent with those of Scarsoglio et al. (2013) who analyzed the precipitation data at the global scale clearly show that the spatial boundary effects were minimized in our study. This means the approach developed by Rheinwalt et al. (2012) was effective and accurate. Fig. 3 also shows the hubs in the ESSTEs network detected in the Atlantic and Pacific oceans between 30° and 60° North. More specifically, we observed hubs off the Eastern Coast of the United States, surrounding the United Kingdom, in the Baltic Sea, in the Mediterranean and Red Seas, the Sea of Japan, East China Sea, and the Sea of Okhotsk.

Climatologically, the high k values in regions like Northwestern Mexico, the southwestern coast of India, North-Northeastern China, and Mongolia likely result from orographic effects and monsoonal dynamics. Orography enhances localized convection and, together with large-scale atmospheric flows, modulates teleconnections (Adam et al., 2006; Shige, 2016). In Africa, the extensive band of high k suggests that the African Easterly Jet and associated regional teleconnections (e.g., ENSO and IOD) are key drivers of synchronous precipitation extremes (Nicholson, 2013). Along the eastern coast of the United States, the United Kingdom, and adjacent seas, high k hubs coincide with major oceanic boundary current systems such as the Gulf Stream and Kuroshio Current, which anchor persistent SST anomalies and influence teleconnections (Deser et al., 2010; NOAA Climate.gov).

Mondal et al. (2020) and Jamali et al. (2023) analyzed daily precipitation data, constructed EPE networks and reported hubs in Northeast and North CONUS for the June-July-August season. In this study, we, however, did not detect any hub in such regions in the US. This can be because our network was constructed based on monthly precipitation data and their extreme values, while both Mondal et al. (2020) and Jamali et al. (2023) used daily precipitation data. This also means extreme precipitation events in Northeast and North of CONUS are probably synchronized at shorter time scales (daily instead of monthly).

While many articles on SST hubs do exist, we take a novel approach by analyzing extreme values in SST data. Therefore, we compare here our ESSTE network hubs against findings of (Tantet and Dijkstra, 2014) see their Fig.1, which displays strong SST hubs in the Indian Ocean, and from 0° N 180° W to 15° N, 75° W, and along the Pacific coast of the US and Canada. Of note is that counter to our own findings, moderate to weak SST hubs were found in the locations we found strong ESSTE hubs, except for in the case of our East Asian hubs, which match closely with their findings. It is important to note how the difference in network construction between ESSTEs and SSTs may highlight incongruities in climatological processes.

3.2.2. Mean geographic distance

Mean geographic distance (MGD) quantifies the average physical (or geographic) distance between directly connected nodes in a network. High MGD values indicate that connected nodes in a network are, on average, far apart, meaning that the network is spatially extensive, and interactions span large areas.

In Fig. 4, we show the spatial variation of MGDs within the Northern Hemisphere (0-60°) for both EPE and ESSTE networks using τ_{max} = 0. For the EPEs network, we found high MGD values in Northwestern Mexico extending through Arizona, New Mexico, and into Colorado -

with isolated high values on the East Coast (North Carolina and West Virginia). Interestingly, Jamali et al. (2023), who analyzed daily precipitation data and studied EPEs in the CONUS, also reported high MGDs in California and Arizona for the June-July-August season (see their Fig. 5). Consistencies between our monthly-based analyses and their daily-based ones indicate that extreme precipitation events in California and Arizona show similar synchronization patterns.

We also observed regions with high MGD values extended from Southern Mexico up to the entire Pacific Coast of the US and Canada. Some high MGDs were also detected in British Columbia and throughout Manitoba in Canada. The northern part of South America also showed high MGDs, particularly in Venezuela. This pattern of high MGD values may be explained by a combination of factors: (1) monsoonal moisture transport from Mexico and the Gulf of California into the US, (2) atmospheric rivers enhancing the EPEs on the Pacific Coast, (3) mesoscale and synoptic-scale circulations from the North Tropical Atlantic and Caribbean Low-Level Jet to Venezuela (Adams and Comrie, 1997; Dettinger, 2011; Tim and Bravo de Guenni, 2015).

For the African Sahel, we found intermediate MGDs (Fig. 4). Given that this region had high degrees, the intermediate MGDs indicate local and regional connections. In the south of the Sahel, we, however, found high MGDs, dominantly in Nigeria, Cameroon, and Ethiopia.

Within Eurasia, we see high MGDs in Austria, Romania, the Caucuses around Georgia, Kyrgyzstan, Tajikistan, East India, Southeastern China, and North Korea. The observed high Mean Geographic Distances (MGDs) in regions such as Austria, Romania, the Caucasus (around Georgia), Kyrgyzstan, Tajikistan, East India, Southeastern China, and North Korea can be attributed to several climatic and topographical factors that influence precipitation patterns over extensive areas. Within South and East Asia, long-range connections are made via the western

North Pacific–North America pattern, which includes the Western Pacific subtropical high (Ha et al., 2017). The orogenic effect of the Caucus mountains, along with the climatological influence from the Siberian High creates a disconnect between the precipitation experienced in the nearby countries, and the source of the precipitation, as found by (Forte et al., 2016). Similar phenomena have been found to influence Austria via the Alps, and precipitation shadows have been found to cause discontinuities in precipitation measurements in the Carpathian mountains which surround Romania (Isotta et al., 2013; Janusz et al., 2019).

For the ESSTEs network, the MGD values were generally low, with some exceptions i.e., areas from 0˚ to 15˚N, 180˚W to 90˚W, and from about 150˚ to 180˚E of about the same latitude. The nature of MGD suggests that nodes within the darker regions are influenced by teleconnection to another non-local node and have a high likelihood of being involved in spatially distant propagation of atmospheric conditions. Conversely, locations within the map that exhibit a lighter coloring are indicative of local influence.

Climatologically for ESSTEs, the generally low MGD values imply that extreme SST events are predominantly controlled by localized oceanic processes—such as coastal upwelling, thermocline adjustments, and air-sea interactions. However, the higher MGD exceptions indicate regions where remote climatic drivers (e.g., ENSO or the Western Pacific Warm Pool) impose long-range synchronization patterns on SST extremes.

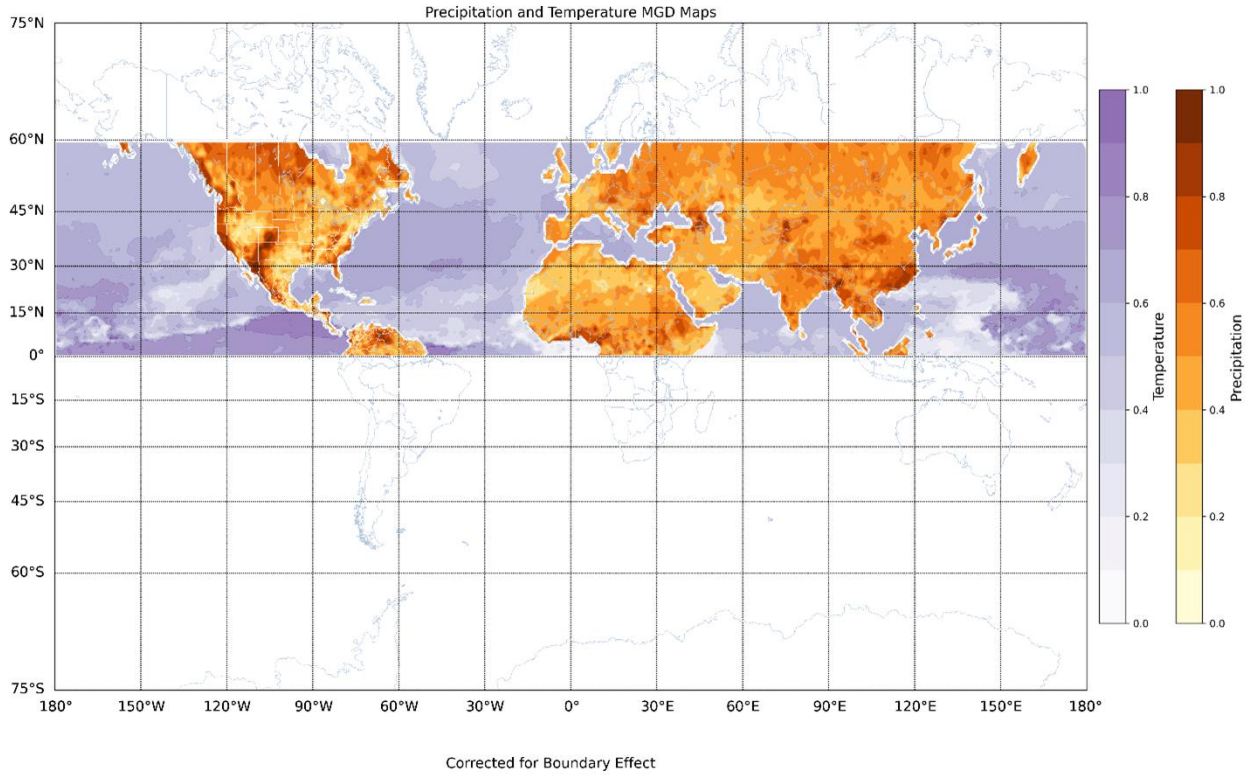

Figure 4 Mean geographic distance, corrected for spatial boundary effects, within the Northern Hemisphere (0-60° North) for the EPEs and ESSTEs from 1930 to 2020. Results for EPEs are shown with warm tones (right scale), while for ESSTEs with cool tones (left scale). The numerical scale is the same for both, ranging from 0 to 1. The map outside of the study area is empty and used only to show relation to the study area.

Overall, these MGD findings reflect the dual influence of local and distant drivers in both precipitation and SST extremes. Ocean currents play a crucial role in redistributing heat and moisture globally.

3.2.3. Clustering coefficient

Clustering Coefficient provides insight into how tightly knit a group of nodes is, reflecting the local cohesion within the network. A node with a high C_c value has strong local interconnectivity (Mondal et al., 2020). The spatial variation of the C_c in the Northern Hemisphere for the JJASON with $\tau_{max} = 0$ months are presented in Fig. 5. Results for both EPE and ESSTE networks are represented.

In Fig. 5, we show the clustering coefficient spatial variation for both the EPE the ESSTE networks. Within the EPE network, North America contains mostly low to moderate C_c values, with small patches of high C_c in the Pacific Northwest, and in localized areas of Western and Eastern Texas, Alabama, Maryland, and New Hampshire. In Africa, moderate to high C_c values extend from Western West Africa through Central Africa and into the Eastern coast of Northern Africa, with specific regions (e.g., Western Sahara, Niger, Chad) exhibiting very high local clustering. This pattern of high local cohesion continues north and east into the Middle East and Kazakhstan.

Climatologically, high C values in Africa suggest that strong local interactions—driven by the African Easterly Jet, surface heating, and convective processes—result in closely linked precipitation patterns (Nicholson, 2013; Cook, 1999). In North America, moderate C values in the Pacific Northwest and the East Coast indicate that while there is some degree of local synchronization, these areas are less influenced by robust local processes and may instead be impacted by larger-scale phenomena. Notably, Bracken et al. (2015) observed in the Pacific Northwest that the moderate clustering reflects a balance between local convective dynamics and remote influences, such as those modulated by ENSO conditions.

In the Tropical Pacific (180˚W–75˚W), high C_c values indicate that the localized dynamics of SSTs—driven by thermocline interactions and ENSO feedback mechanisms—reinforce synchronous variability over relatively compact areas (Giannakis & Slawinska, 2016). Similarly high values are found south of Greenland, south of West Africa, and from Western India to east of Vietnam. Similarly, regions south of Greenland and West Africa exhibit high SST clustering, reflecting localized ocean–atmosphere coupling that shapes regional climate extremes (Deser et al., 2010). Thus, while low $C_c$values imply a reliance on broad teleconnections for synchronizing

extreme events, high C_c values are characteristic of areas where local interactions dominate the response to climatic forcing.

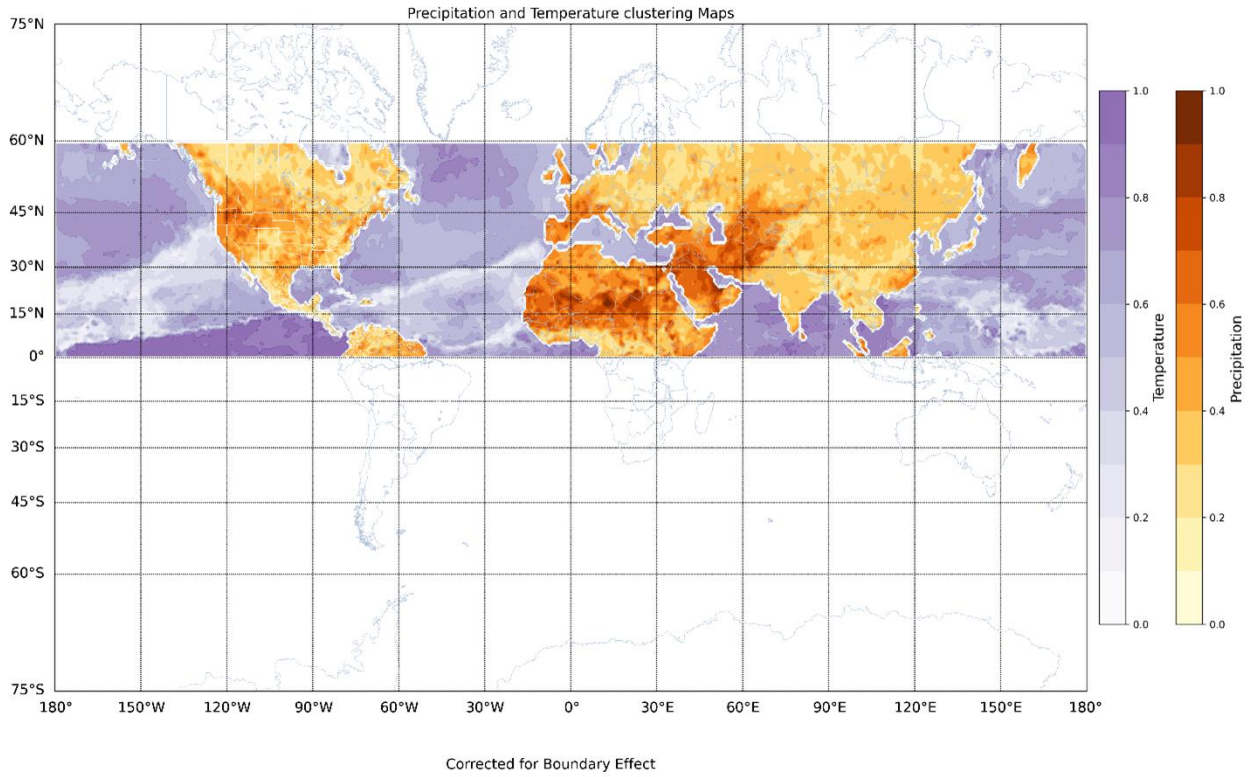

Figure 5 Clustering coefficient, corrected for spatial boundary effects, within the Northern Hemisphere for the EPEs and ESSTEs from 1930 to 2020. Results for the EPEs are shown with warm tones (right scale), while for the ESSTEs with cool tones (left scale). The numerical scale is the same for both, ranging from 0 to 1. The map outside of the study area is empty and used only to show relation to the study area.

The patterns revealed by our network analysis emphasize the importance of underlying climatic mechanisms which drive extreme events. For example, the presence of synchronization hubs in the African Sahel and parts of Asia reflects the role of known atmospheric circulation patterns such as the African Easterly Jet and monsoonal systems. Similarly, SST hubs in regions influenced by the Gulf Stream and the Kuroshio Current highlight the importance of oceanic boundary currents in anchoring persistent SST events. These physical drivers help explain the observed clustering of extremes. The contrast in spatial coherence and mean geographic distance between EPEs and ESSTEs further demonstrates differences in how terrestrial and oceanic

systems respond to climatic forcing. By linking these observed patterns to known atmospheric and oceanic mechanisms, our results provide insights that may enhance forecasting of extreme events and support regional adaptation strategies.

Chapter 4 - Conclusion

In this study, we explored the use of complex network theory to analyze the spatiotemporal patterns of extreme precipitation events (EPEs) and extreme sea surface temperature events (ESSTEs) from the equator to 60˚N latitude in the Northern Hemisphere. Extremity of precipitation and sea surface temperature events was determined by the 95th percentile threshold at each node. The event synchronization (ES) method was used to calculate the similarity between the extreme event series, and the EPEs and ESSTEs complex networks were constructed by setting $\tau_{max} = 0$ months. We then calculated the network measures (degree (k), mean geographic distance (MGD), and clustering coefficient (C_c)), all corrected for the spatial boundary effects. Hubs of extreme precipitation were discovered in Mexico, African Sahel, and in several locations in Asia. The MGD results for the EPEs network indicated that the following locations participated in geographically distant connections: Pacific North America, East Coast United States, Venezuela, Western Central and Eastern Africa, Georgia, Kyrgyzstan, East India, Vietnam, and Southwestern China. The MGD values within the ESSTEs network were generally low, with exceptions off the Southern Coast of Mexico, the Eastern Coast of French Guiana, and sparsely from about 140˚E - 165˚E and 0˚N - 15˚N. Within the EPE network, spatial coherence, determined through clustering coefficient calculations, was strongest across Africa and into the Middle East, with some moderately high to high values in the Northwestern and Northeastern US, and the UK. The C_c values obtained from the ESSTEs network were highest in regions dominated by strong ocean-atmosphere interactions, including the Indian Ocean, East China Sea, Sea of Japan, and appearing south of Mexico in a spatial pattern that contrasts with our MGD values. This relationship suggests that while some extreme events propagate over large distances, others remain constrained by strong localized influences. These

findings reinforce the ability of complex network theory to identify both regional and global synchronization structures within climate extremes. By quantifying connectivity, spatial extent, and clustering of extreme events, we demonstrated how network measures provide insight into the mechanisms governing climate variability. Our results further illustrate the contrast between terrestrial and marine extremes, where precipitation hubs are strongly tied to atmospheric circulation and orographic effects, while SST hubs align with major ocean currents and teleconnections. This distinction underscores the necessity of integrating both terrestrial and oceanic influences when modeling extreme climate events. Contrasting our results of terrestrial and marine extremes offers valuable insight for future improvements to predictive climatological models and strategies for regional adaptation.

References

A primer for EOF analysis of climate data ResearchGate, https://www.researchgate.net/publication/228781584_A_primer_for_EOF_analysis_of_climate_data (accessed January 2025).

Adam, J.C., Clark, E.A., Lettenmaier, D.P., and Wood, E.F., 2006, Correction of global precipitation products for orographic effects: Journal of Climate, v. 19, p. 15–38, doi:10.1175/JCLI3604.1.

Adams, D.K., and Comrie, A.C., 1997, The North American Monsoon:, https://journals.ametsoc.org/view/journals/bams/78/10/1520-0477_1997_078_2197_tnam_2_0_co_2.xml (accessed January 2025).

Agel, L., Barlow, M., Qian, J.-H., Colby, F., Douglas, E., and Eichler, T., 2015, Climatology of Daily Precipitation and Extreme Precipitation Events in the Northeast United States:, doi:10.1175/JHM-D-14-0147.1.

Alexander, L.V., 2016, Global observed long-term changes in temperature and precipitation extremes: A review of progress and limitations in IPCC assessments and beyond: Weather and Climate Extremes, v. 11, p. 4–16, doi:10.1016/j.wace.2015.10.007.

Bjerknes, J., 1969, ATMOSPHERIC TELECONNECTIONS FROM THE EQUATORIAL PACIFIC:, https://journals.ametsoc.org/view/journals/mwre/97/3/1520-0493_1969_097_0163_atftep_2_3_co_2.xml (accessed January 2025).

Boers, N., Bookhagen, B., Marwan, N., and Kurths, J., 2016, Spatiotemporal characteristics and synchronization of extreme rainfall in South America with focus on the Andes Mountain range: Climate Dynamics, v. 46, p. 601–617, doi:10.1007/s00382-015-2601-6.

Boers, N., Goswami, B., Rheinwalt, A., Bookhagen, B., Hoskins, B., and Kurths, J., 2019, Complex networks reveal global pattern of extreme-rainfall teleconnections: Nature, v. 566, p. 373–377, doi:10.1038/s41586-018-0872-x.

Bracken, C., Rajagopalan, B., Alexander, M., and Gangopadhyay, S., 2015, Spatial variability of seasonal extreme precipitation in the western United States: Journal of Geophysical Research: Atmospheres, v. 120, p. 4522–4533, doi:10.1002/2015JD023205.

Buishand, T. a., 1989a, Statistics of extremes in climatology: Statistica Neerlandica, v. 43, p. 1–30, doi:10.1111/j.1467-9574.1989.tb01244.x.

Buishand, T. a., 1989b, Statistics of extremes in climatology: Statistica Neerlandica, v. 43, p. 1–30, doi:10.1111/j.1467-9574.1989.tb01244.x.

Ceron, K., Santana, D.J., and Valente-Neto, F., 2020, Seasonal patterns of ecological uniqueness of anuran metacommunities along different ecoregions in Western Brazil: PLOS ONE, v. 15, p. e0239874, doi:10.1371/journal.pone.0239874.

Climate Change, Atmospheric Rivers, and Floods in California – A Multimodel Analysis of Storm Frequency and Magnitude Changes1 - Dettinger - 2011 - JAWRA Journal of the American Water Resources Association - Wiley Online Library, https://onlinelibrary.wiley.com/doi/10.1111/j.1752-1688.2011.00546.x (accessed March 2025).

Climate Variability: North Atlantic Oscillation | NOAA Climate.gov, 2009, http://www.climate.gov/news-features/understanding-climate/climate-variability-north-atlantic-oscillation (accessed January 2025).

Decoupling of modern shortening rates, climate, and topography in the Caucasus - ScienceDirect, https://www.sciencedirect.com/science/article/pii/S0012821X16303004#br0290 (accessed March 2025).

Deser, C., Alexander, M.A., Xie, S.-P., and Phillips, A.S., 2010, Sea surface temperature variability: patterns and mechanisms: Annual Review of Marine Science, v. 2, p. 115–143, doi:10.1146/annurev-marine-120408-151453.

Diffenbaugh, N.S. et al., 2017, Quantifying the influence of global warming on unprecedented extreme climate events: Proceedings of the National Academy of Sciences, v. 114, p. 4881–4886, doi:10.1073/pnas.1618082114.

Donges, J.F., Zou, Y., Marwan, N., and Kurths, J., 2009a, Complex networks in climate dynamics: The European Physical Journal Special Topics, v. 174, p. 157–179, doi:10.1140/epjst/e2009-01098-2.

Donges, J.F., Zou, Y., Marwan, N., and Kurths, J., 2009b, The backbone of the climate network: Europhysics Letters, v. 87, p. 48007, doi:10.1209/0295-5075/87/48007.

Ekhtiari, N., Agarwal, A., Marwan, N., and Donner, R.V., 2019, Disentangling the multi-scale effects of sea-surface temperatures on global precipitation: A coupled networks approach: Chaos (Woodbury, N.Y.), v. 29, p. 063116, doi:10.1063/1.5095565.

Falga, R., and Wang, C., 2022, The rise of Indian summer monsoon precipitation extremes and its correlation with long-term changes of climate and anthropogenic factors: Scientific Reports, v. 12, p. 11985, doi:10.1038/s41598-022-16240-0.

Feldhoff, J.H., Lange, S., Volkholz, J., Donges, J.F., Kurths, J., and Gerstengarbe, F.-W., 2015, Complex networks for climate model evaluation with application to statistical versus dynamical modeling of South American climate: Climate Dynamics, v. 44, p. 1567–1581, doi:10.1007/s00382-014-2182-9.

Fellini, S., Salizzoni, P., Soulhac, L., and Ridolfi, L., 2019, Propagation of toxic substances in the urban atmosphere: A complex network perspective: Atmospheric Environment, v. 198, p. 291–301, doi:10.1016/j.atmosenv.2018.10.062.

Forte, A.M., Whipple, K.X., Bookhagen, B., and Rossi, M.W., 2016a, Decoupling of modern shortening rates, climate, and topography in the Caucasus: Earth and Planetary Science Letters, v. 449, p. 282–294, doi:10.1016/j.epsl.2016.06.013.

Forte, A.M., Whipple, K.X., Bookhagen, B., and Rossi, M.W., 2016b, Decoupling of modern shortening rates, climate, and topography in the Caucasus: Earth and Planetary Science Letters, v. 449, p. 282–294, doi:10.1016/j.epsl.2016.06.013.

Giannakis, D., and Majda, A.J., 2012, Nonlinear Laplacian spectral analysis for time series with intermittency and low-frequency variability: Proceedings of the National Academy of Sciences, v. 109, p. 2222–2227, doi:10.1073/pnas.1118984109.

Giannakis, D., and Slawinska, J., 2016, Indo-Pacific variability on seasonal to multidecadal timescales. Part II: Multiscale atmosphere-ocean linkages:, doi:10.48550/arXiv.1609.09185.

Ha, K.-J., Seo, Y.-W., Lee, J.-Y., Kripalani, R.H., and Yun, K.-S., 2018, Linkages between the South and East Asian summer monsoons: a review and revisit: Climate Dynamics, v. 51, p. 4207–4227, doi:10.1007/s00382-017-3773-z.

Halverson, M.J., and Fleming, S.W., 2015, Complex network theory, streamflow, and hydrometric monitoring system design: Hydrology and Earth System Sciences, v. 19, p. 3301–3318, doi:10.5194/hess-19-3301-2015.

Hansen, J., Ruedy, R., Sato, M., and Lo, K., 2010, Global Surface Temperature Change: Reviews of Geophysics, v. 48, doi:10.1029/2010RG000345.

Held, I.M., and Soden, B.J., 2006, Robust Responses of the Hydrological Cycle to Global Warming:, doi:10.1175/JCLI3990.1.

Jamali, T., Ghanbarian, B., and Kurths, J., 2023, Spatiotemporal analysis of extreme precipitation events in the United States at mesoscale: Complex network theory: Journal of Hydrology, v. 627, p. 130440, doi:10.1016/j.jhydrol.2023.130440.

Kim, K., Jung, J., Kim, H.S., Haraguchi, M., and Kim, S., 2022, Rainfall pattern analysis in 24 East Asian megacities using a complex network: Hydrology and Earth System Sciences, v. 26, p. 4823–4836, doi:10.5194/hess-26-4823-2022.

Kotz, M., Levermann, A., and Wenz, L., 2022, The effect of rainfall changes on economic production: Nature, v. 601, p. 223–227, doi:10.1038/s41586-021-04283-8.

Kozak, J., Cebulak, D., Stec, T., and Jaguś, A., 2019, Variation of Precipitation Gradient in Mountain Areas Based on the Example of the Western Beskids in the Polish Carpathians: Journal of Ecological Engineering, v. Vol. 20, doi:10.12911/22998993/112502.

Li, Y., 2023, A spatiotemporal oscillator model for ENSO:, doi:10.48550/arXiv.2306.04074.

Malik, N., Bookhagen, B., Marwan, N., and Kurths, J., 2012, Analysis of spatial and temporal extreme monsoonal rainfall over South Asia using complex networks: Climate Dynamics, v. 39, p. 971–987, doi:10.1007/s00382-011-1156-4.

Metcalfe, S.E., Barron, J.A., and Davies, S.J., 2015, The Holocene history of the North American Monsoon: 'known knowns' and 'known unknowns' in understanding its spatial and temporal complexity: Quaternary Science Reviews, v. 120, p. 1–27, doi:10.1016/j.quascirev.2015.04.004.

Molkenthin, N., Kutza, H., Tupikina, L., Marwan, N., Donges, J.F., Feudel, U., Kurths, J., and Donner, R.V., 2017, Edge anisotropy and the geometric perspective on flow networks: Chaos: An Interdisciplinary Journal of Nonlinear Science, v. 27, p. 035802, doi:10.1063/1.4971785.

Monselesan, D.P. et al., 2024, On the archetypal `flavours', indices and teleconnections of ENSO revealed by global sea surface temperatures:, doi:10.48550/arXiv.2406.08694.

Murgulet, D., Valeriu, M., Hay, R.R., Tissot, P., and Mestas-Nuñez, A.M., 2017, Relationships between sea surface temperature anomalies in the Pacific and Atlantic Oceans and South Texas precipitation and streamflow variability: Journal of Hydrology, v. 550, p. 726–739, doi:10.1016/j.jhydrol.2017.05.041.

Nicholson, S.E., 2013, The West African Sahel: A Review of Recent Studies on the Rainfall Regime and Its Interannual Variability: International Scholarly Research Notices, v. 2013, p. 453521, doi:10.1155/2013/453521.

Nicholson, S.E., and Dezfuli, A.K., 2013, The Relationship of Rainfall Variability in Western Equatorial Africa to the Tropical Oceans and Atmospheric Circulation. Part I: The Boreal Spring:, doi:10.1175/JCLI-D-11-00653.1.

Nigam, S., and Baxter, S., 2015, GENERAL CIRCULATION OF THE ATMOSPHERE | Teleconnections, *in* North, G.R., Pyle, J., and Zhang, F. eds., Encyclopedia of Atmospheric Sciences (Second Edition), Oxford, Academic Press, p. 90–109, doi:10.1016/B978-0-12-382225-3.00400-X.

Pan, X., Wang, W., Liu, T., Akmalov, S., De Maeyer, P., and Van de Voorde, T., 2022, Integrated modeling to assess the impact of climate change on the groundwater and surface water in the South Aral Sea area: Journal of Hydrology, v. 614, p. 128641, doi:10.1016/j.jhydrol.2022.128641.

Pendergrass, A.G., 2018, What precipitation is extreme? Science, doi:10.1126/science.aat1871.

Roxy, M., 2014, Sensitivity of precipitation to sea surface temperature over the tropical summer monsoon region—and its quantification: Climate Dynamics, v. 43, p. 1159–1169, doi:10.1007/s00382-013-1881-y.

Rummukainen, M., 2012, Changes in climate and weather extremes in the 21st century: WIREs Climate Change, v. 3, p. 115–129, doi:10.1002/wcc.160.

Scarsoglio, S., Laio, F., and Ridolfi, L., 2013, Climate Dynamics: A Network-Based Approach for the Analysis of Global Precipitation: PLOS ONE, v. 8, p. e71129, doi:10.1371/journal.pone.0071129.

Shige, S., and Kummerow, C.D., 2016, Precipitation-Top Heights of Heavy Orographic Rainfall in the Asian Monsoon Region:, doi:10.1175/JAS-D-15-0271.1.

Simple Algorithms for Peak Detection in Time-Series ResearchGate, https://www.researchgate.net/publication/228853276_Simple_Algorithms_for_Peak_Detection_in_Time-Series (accessed January 2025a).

Simple Algorithms for Peak Detection in Time-Series, https://www.researchgate.net/publication/228853276_Simple_Algorithms_for_Peak_Detection_in_Time-Series?enrichId=rgreq-8946388e7040e69e344e43baf2f02935-XXX&enrichSource=Y292ZXJQYWdlOzIyODg1MzI3NjtBUzoxMzQ2NjY1MjI3MzA0OThAMTQwOTExODQwOTk5Ng%3D%3D&el=1_x_2 (accessed January 2025b).

Steinhaeuser, K., Chawla, N.V., and Ganguly, A.R., 2009, An exploration of climate data using complex networks, *in* Proceedings of the Third International Workshop on Knowledge Discovery from Sensor Data, New York, NY, USA, Association for Computing Machinery, SensorKDD '09, p. 23–31, doi:10.1145/1601966.1601973.

Sun, H., and Furbish, D.J., 1997, Annual precipitation and river discharges in Florida in response to El Niño- and La Niña-sea surface temperature anomalies: Journal of Hydrology, v. 199, p. 74–87, doi:10.1016/S0022-1694(96)03303-3.

Taboada, F.G., and Anadón, R., 2012, Patterns of change in sea surface temperature in the North Atlantic during the last three decades: beyond mean trends: Climatic Change, v. 115, p. 419–431, doi:10.1007/s10584-012-0485-6.

Tantet, A., and Dijkstra, H.A., 2014, An interaction network perspective on the relation between patterns of sea surface temperature variability and global mean surface temperature: Earth System Dynamics, v. 5, p. 1–14, doi:10.5194/esd-5-1-2014.

Thackeray, C.W., Hall, A., Norris, J., and Chen, D., 2022, Constraining the increased frequency of global precipitation extremes under warming: Nature Climate Change, v. 12, p. 441–448, doi:10.1038/s41558-022-01329-1.

The climate of daily precipitation in the Alps: Development and analysis of a high-resolution grid dataset from pan-Alpine rain-gauge data ResearchGate, https://www.researchgate.net/publication/256112141_The_climate_of_daily_precipitation_in_the_Alps_Development_and_analysis_of_a_high-resolution_grid_dataset_from_pan-Alpine_rain-gauge_data (accessed March 2025).

The North American Monsoon ResearchGate, https://www.researchgate.net/publication/260730829_The_North_American_Monsoon (accessed March 2025).

Tim, N., and Bravo de Guenni, L., 2016a, Oceanic influence on the precipitation in Venezuela under current and future climate: Climate Dynamics, v. 47, p. 211–234, doi:10.1007/s00382-015-2832-6.

Tim, N., and Bravo de Guenni, L., 2016b, Oceanic influence on the precipitation in Venezuela under current and future climate: Climate Dynamics, v. 47, p. 211–234, doi:10.1007/s00382-015-2832-6.

Trenberth, K.E., and Shea, D.J., 2005, Relationships between precipitation and surface temperature: Geophysical Research Letters, v. 32, doi:10.1029/2005GL022760.

Trends in Intense Precipitation in the Climate Record ResearchGate, https://www.researchgate.net/publication/239803522_Trends_in_Intense_Precipitation_in_the_Climate_Record (accessed January 2025).

Walsh, K.J.E. et al., 2016, Tropical cyclones and climate change: WIREs Climate Change, v. 7, p. 65–89, doi:10.1002/wcc.371.

Wu, R., 2019, Summer precipitation–SST relationship on different time scales in the northern tropical Indian Ocean and western Pacific: Climate Dynamics, v. 52, p. 5911–5926, doi:10.1007/s00382-018-4487-6.

Wu, R., Kirtman, B.P., and Pegion, K., 2008, Local rainfall-SST relationship on subseasonal time scales in satellite observations and CFS: Geophysical Research Letters, v. 35, doi:10.1029/2008GL035883.